ISSN 1388-0764, Volume 12, Number 7

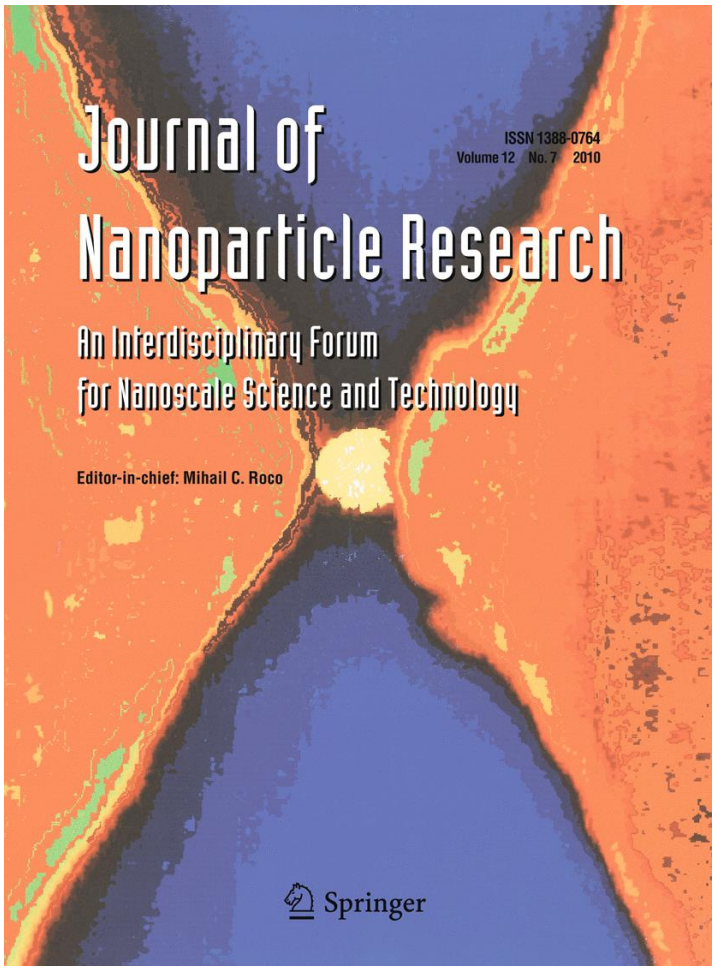

J Nanopart Res (2010) 12:2553–2565
DOI 10.1007/s11051-009-9824-6

RESEARCH PAPER

Uniform YF_3:Yb,Er up-conversion nanophosphors of various morphologies synthesized in polyol media through an ionic liquid

Nuria O. Nuñez · Marta Quintanilla · Eugenio Cantelar · Fernando Cussó · Manuel Ocaña

Received: 21 July 2009 / Accepted: 28 November 2009 / Published online: 10 December 2009

Abstract We describe a facile procedure for the synthesis at low temperature (120 °C) of water-dispersible uniform YF_3:Yb,Er up-conversion nanophosphors of various morphologies (rhombic and spheroidal) by homogeneous precipitation in polyol solutions containing different lanthanide salts and an ionic liquid (1-butyl, 2-methylimidazolium tetrafluoroborate) as fluoride source. It is shown that the shape of the obtained nanoparticles is mainly determined by the nature of both, the polyol and the lanthanide precursors, which also affects to their colloidal stability in water suspensions. These morphological differences are explained on the basis of a different mechanism of particle formation. The efficiency of the up-conversion processes in the synthesized rhombic and spheroidal nanoparticles is also comparatively analyzed and the observed differences are justified on the basis of the different impurities incorporated to the nanophosphors during their synthesis process.

Keywords Nanoparticles · Luminescence · Rare earth · Yttrium fluoride · Up-conversion

N. O. Nuñez · M. Ocaña (✉)
Instituto de Ciencia de Materiales de Sevilla, CSIC-US, Americo Vespucio 49, 41092 Isla de la Cartuja, Sevilla, Spain
e-mail: mjurado@icmse.csic.es

M. Quintanilla · E. Cantelar · F. Cussó
Depto. Física de Materiales, C-IV, Universidad Autónoma de Madrid, Madrid, Spain

Introduction

Up-conversion (UC) fluorescent materials emit visible light after absorbing lower-energy (near-infrared) photons. Due to this property, they find important applications in different fields of science and technology such as optoelectronic (solid state lasers (Scheps 1996), solar cells (Shalav et al. 2005), flat-panel displays (Downing et al. 1996)) and biotechnology (Yi et al. 2004). Their use as biolabels is of special interest owing to the important advantages that UC phosphors present over the conventional down-conversion ones, which include high light penetration depth in tissues, no photodamage to living organisms, weak auto-fluorescence from cells or tissues, low background light and high sensitivity for detection (Yi and Chow 2006; Li and Zhang 2008). For many of these applications, the availability of uniform nanoparticles with controlled size, shape and good dispersiblity (in water for biolabelling) and strong emission is highly desirable (Yi et al. 2004; Wang 2006; Wang et al. 2007; Sun et al. 2007; Nuñez et al. 2008).

The most studied UC phosphors are based on lanthanide (mainly La or Y) compounds co-doped with Yb and Er (green emitting) or Tm (blue emitting) cations. In these systems, the presence of Yb^{3+}, which acts as a sensitizer, remarkably enhances the Er^{3+} or Tm^{3+} emission through energy transfers from the Yb^{3+} to the Er^{3+} or Tm^{3+} excited states (Sun et al. 2007). The choice of the host material is also a very important issue. Thus, fluorides are more preferred

than oxides as the former have lower vibrational energies and consequently, the quenching of the exited state of the Ln cations is minimized, resulting in a higher quantum efficiency of luminescence (Stouwdam and van Veggel 2002; Yan and Li 2005). Among all studied Ln fluoride host materials, $NaYF_4$, LaF_3 and YF_3 are considered as the most efficient ones (Yi and Chow 2005). Although a great research effort have been recently conducted to develop synthesis routes to produce uniform nanoparticles in the two-first cases (Yi et al. 2004; Yi and Chow 2006; Wang et al. 2007; Sun et al. 2007; Yi and Chow 2005; Wang and Li 2007; De et al. 2005; Zhang et al. 2009), less attention has been paid to the YF_3-based UC nanophosphors (Wang et al. 2009). In fact, most of the few synthesis procedures published for this material resulted in particles in the micrometre ($\gg$100 nm) size range (Yan and Li 2005; Cao et al. 2008; Wang et al. 2008) or in strongly aggregated nanoparticles (Yan and Li 2005; Cao et al. 2008; Cui et al. 2006).

In a previous work, we reported a simple and environmentally friendly procedure for the synthesis of uniform yttrium fluoride nanoparticles with rhombic shape (longer axis = 130 nm, shorter axis = 54 nm and thickness = 23 nm) by homogeneous precipitation in ethylene glycol solutions using an ionic liquid (1-butyl, 3-methylimidazolium tetrafluoroborate, $[BMIM]BF_4$) as fluoride source (Nuñez and Ocaña 2007). This method was found to require very restrictive experimental conditions to obtain uniform nanoparticles involving the use of yttrium acetate (0.02 mol dm^{-3}) as lanthanide source and a high concentration (2.7 mol dm^{-3}) of the ionic liquid. The use of other inorganic yttrium salts or lower ionic liquid (IL) concentrations gave rise to irregular and/or highly agglomerate systems. In this article, we describe a modification of this procedure, which permits the synthesis of uniform water-dispersible Yb, Er co-doped YF_3 nanoparticles whose shape, size and structural features can be tuned by changing the nature of both, the polyol solvent and the lanthanide precursors, which also affect their colloidal stability in water and their luminescent properties. This new procedure also involves the use of a common yttrium salt (chloride) and a much lower amount of $[BMIM]BF_4$, which is also interesting from the economic point of view. The origin of the different luminescent behaviour of the here prepared nanophosphors is also studied in detail.

Experimental section

Reagents

Yttrium(III) acetate (YOAc, $Y(CH_3COO)_3{\cdot}XH_2O$, Aldrich, 99.9%), yttrium(III) chloride hexahydrate ($YCl_3{\cdot}6H_2O$, Aldrich, 99.9%), erbium(III) acetylacetonate ($Er(CH_3COCHCOCH_3)_3$, Alpha Aesar, 99.9%), erbium(III) chloride hexahydrate ($ErCl_3{\cdot}6H_2O$, Aldrich, 99.9%), ytterbium(III) acetylacetonate ($Yb(CH_3COCHCOCH_3)_3$, Alpha Aesar, 99.9%) and ytterbium(III) chloride hexahydrate ($YbCl_3{\cdot}6H_2O$, Aldrich, 99.9%) were selected as Ln precursors. 1-Butyl, 3-methylimidazolium tetrafluoroborate, ($[BMIM]BF_4$, $C_8H_{15}BF_4N_2$, Fluka, >97%), was used as fluoride source and ethylene glycol (EG) (Fluka, <99.5%) or diethylene glycol (DEG) (Aldrich, 99%) as solvents. All chemicals were used as-received.

Nanoparticles synthesis

The standard procedure for the synthesis of the yttrium fluoride nanoparticles containing a 2% (molar) of Er^{3+} and a 10% of Yb^{3+} was as follows. Proper amounts of the rare-earth precursors were dissolved in the selected solvent (ethylene or diethylene glycol) under magnetic stirring, heating the vial at $\sim$100 °C to facilitate the dissolution process. These solutions were cooled down to room temperature after which, the desired volume of $[BMIM]BF_4$ was admixed keeping the magnetic stirring. The final solutions (total volume = 10 cm^3) were then aged for 15 h in tightly closed test tubes using an oven preheated at the selected temperature. After ageing, the resulting dispersions were cooled down to room temperature, centrifuged to remove the supernatants and washed, twice with ethanol and once with double distilled water. Finally, the powders were dried at 50 °C.

The powders were thermally treated for 20 min in a furnace heated up to the desired temperature at a heating rate of 10 °C/min.

Characterization

The shape of the nanoparticles was examined by transmission electron microscopy (TEM, Philips 200CM). For this, a droplet of an aqueous suspension of the samples was deposited on a copper grid coated with a transparent polymer and dried. The particle

size distributions were obtained from the micrographs by counting several hundreds of particles.

The composition of the precipitated particles was assessed by energy dispersive X-ray analysis (EDX, Philips DX4) coupled to the TEM microscope.

In order to obtain structural information on the prepared nanoparticles, we used X-ray diffraction (XRD, Siemens D501). Crystallite size was calculated from the reflection at $2\theta = \sim 31°$ by using the Scherrer method.

Thermogravimetric analysis (TGA) was performed in air at a heating rate of 10 °C min^{-1}, using a Q600 TA Instrument.

The infrared spectra of the powders, as-prepared and after heating at 400 °C (heating rate of 10 °C min^{-1}), were recorded in air atmosphere using a FTIR JASCO 6300 spectrometer equipped with a "Praying Mantis" Diffuse Reflectance Infrared Fourier Transform Spectroscopy (DRIFTS) cell.

Temperature programmed desorption (TPD) experiments were carried out using a O_2/He mixture (20% O_2 by volume) and a heating rate of 15 °C/min, holding the sample at 400 °C for 15 min. A mass spectrometer (QMS422-Baltzers) was used to detect the desorption products.

The optical measurements for powdered pressed samples were performed using a JENOPTIK laser diode source at 980 nm to excite the Yb^{3+} ions with different excitation powers. The visible Er^{3+} luminescence was dispersed by using an ARC Spectrapro 500-I monochromator and then detected with a photomultiplier tube. In order to achieve reproducible and comparative luminescence spectra, all the data have been taken using a standard experimental arrangement, including specially design sample holders. They were constructed using a 2-mm thick PMMA spacer with a 3-mm diameter circular opening, enclosed by two microscope slide covers. The nanopowders were introduced filling the cavity, which was placed in a fixed mount on the top of a micrometre stage, in order to optimize the luminescence signal. The diode laser beam was limited by a diaphragm assuring that the excitation area was smaller than the exposed sample area. The sample holder can be removed and replaced into this arrangement without altering the geometry. It has been checked that luminescence spectra are reproducible with integrated intensity variations smaller than a 3%. All emission spectra have been corrected from the response of the monochromator grating and photomultiplier tube.

The emission spectra were transformed to the CIE colour coordinates system using a 2° observer.

Results and discussion

Synthesis and structural characterization

The ageing, under the optimum conditions previously established for undoped YF_3 (Nuñez and Ocaña 2007), of $YOAc_3$/$BMIMBF_4$ solutions containing the desired amounts of $Er(acac)_3$ and $Yb(acac)_3$ in EG (Table 1, sample R) resulted in uniform nanoparticles (Fig. 1a) with a rhombic-like morphology and a mean size (125 × 55 × 23 nm) very similar to those previously reported for the undoped system. The EDX spectrum measured for this sample displayed the main peaks corresponding to Y and F along with

Table 1 Nominal composition, shape and size of YF_3:Yb,Er nanoparticles obtained at 120 °C in different solvents from different Y precursors (0.02 mol dm^{-3}) and variable solvent/IL ratio

	Y(III) precursor	Er(III) precursor	Yb(III) precursor	Er/Y (molar ratio)	Yb/Y (molar ratio)	Solvent	Solvent/IL (volumetric ratio)	Particle shape	Particle size (nm)
Sample R	$YOAc_3$	$Er(acac)_3$	$Yb(acac)_3$	0.02	0.1	EG	2.5/2.5	Rhombic	125 (13) × 55 (6) × 23 (4)
	$YOAc_3$	$Er(acac)_3$	$Yb(acac)_3$	0.02	0.1	DEG	2.5/2.5	Heterogeneous	
	$Y(acac)_3$	$Er(acac)_3$	$Yb(acac)_3$	0.02	0.1	DEG	2.5/2.5	Heterogeneous	
Sample S1	YCl_3	$ErCl_3$	$YbCl_3$	0.02	0.1	DEG	2.5/2.5	Oblate Spheroids	100 (13) × 33 (8)
Sample S2	YCl_3	$ErCl_3$	$YbCl_3$	0.02	0.1	DEG	4.9/0.1	Oblate Spheroids	108 (12) × 46 (5)

The standard deviations are shown in *parentheses*

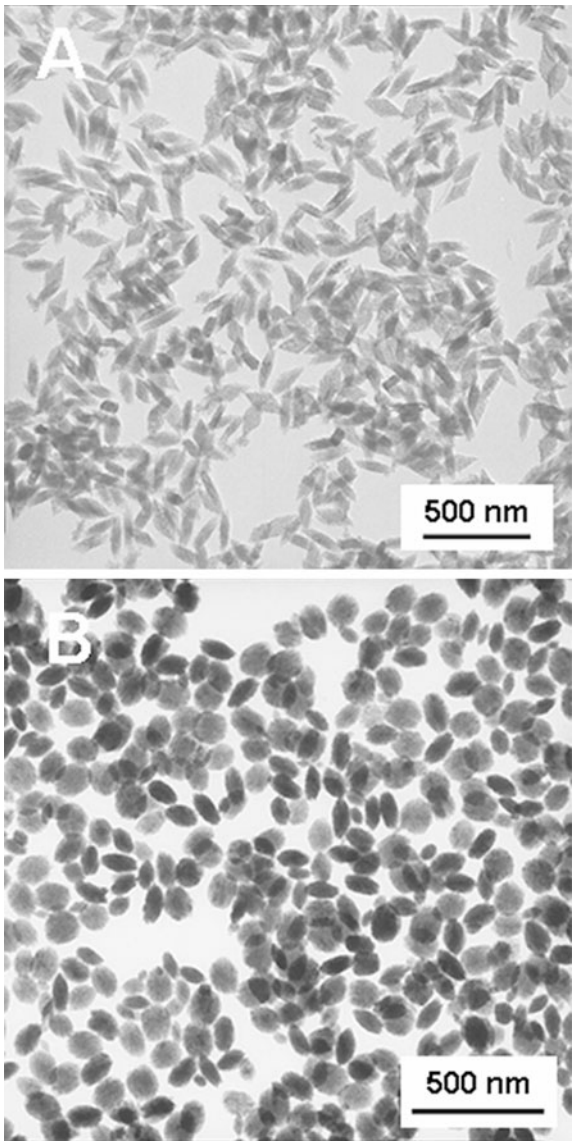

Fig. 1 TEM images of samples R (**a**) and S1 (**b**) prepared under the conditions described in Table 1

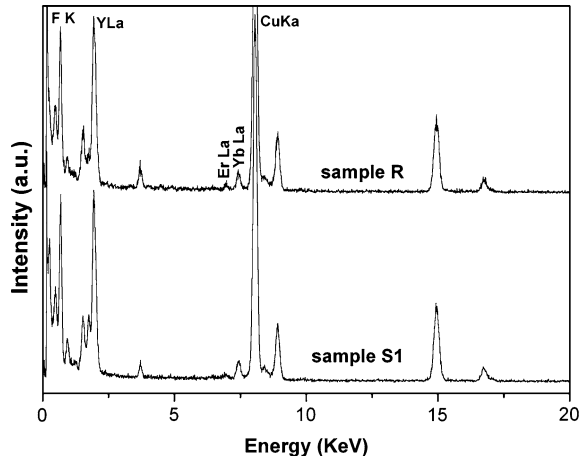

Fig. 2 EDX spectra of samples R and S1. The most intense peak for each element has been labelled

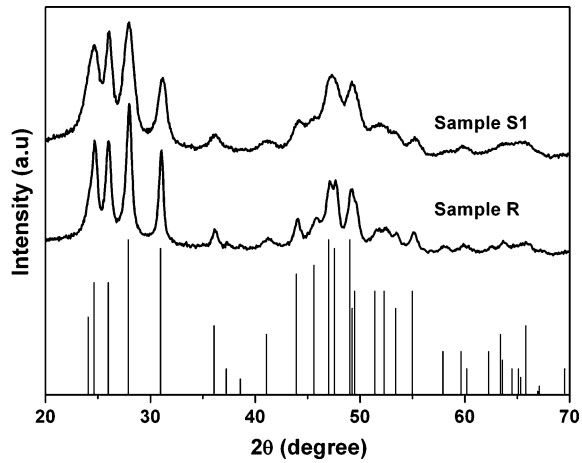

Fig. 3 X-ray diffraction patterns of samples R and S1. The reference pattern for orthorhombic YF_3 (JCPDS file number 32-1431) is also included

others of much lower intensity due to Er and Yb (Fig. 2), which seem to confirm the success of the doping procedure. It should be also noted that the EDX spectra recorded for several single particles were almost identical indicating a high degree of chemical homogeneity in this sample, at least at the particle level. According to XRD (Fig. 3), these nanoparticles were well crystallized and consisted of orthorhombic YF_3 (JCPDS file no. 32-1431).

The change of EG by DEG keeping constant all the other experimental conditions, resulted in tiny irregular and strongly agglomerated nanoparticles. However, when in the DEG system, the yttrium acetate and erbium and ytterbium acetylacetonate precursors were substituted by the corresponding chlorides, homogeneous dispersions could be also obtained but with a different particle shape than that resulted with EG as solvent, as illustrated in Fig. 1b, which corresponds to sample S1 (Table 1). It should be noted that although it seems from the TEM figure that this sample is composed by a mixture of spherical and elongated particles, the higher contrast of the latter suggests a homogeneous morphology so that the apparently spherical particles are in fact

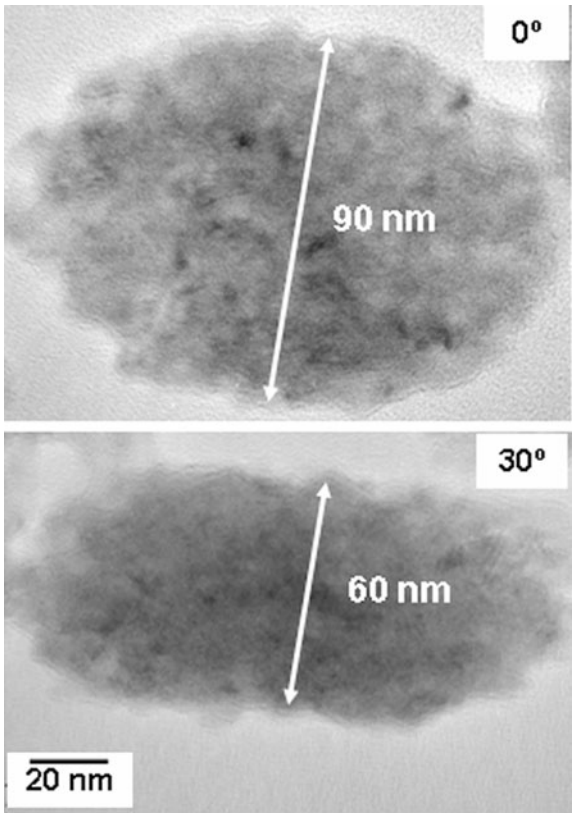

Fig. 4 TEM images taken for a single particle of sample S1 before (0°) and after (30°) tilting the specimen

oblate spheroids lying with their shorter axis perpendicular to the TEM grid plane, whereas those apparently elongated laid with their shorter axis parallel to such plane. This assumption was confirmed by the TEM picture taken for a single particle after tilting the specimen 30° (Fig. 4). As observed, the diameter of this particle was reduced from 90 to 60 nm after rotation clearly demonstrating the oblate spheroidal morphology. The mean dimensions of such spheroids estimated from the TEM pictures were 100 × 33 nm, approximately.

The EDX spectrum obtained for sample S1 was very similar to that of sample R (Fig. 2) showing the F, Y, Er and Yb peaks, which confirms the successful incorporation of the doping cations also into the YF_3 nanospheroids. According to XRD (Fig. 3), the latter also crystallized into the same structure (orthorhombic YF_3) as the rhombic nanoparticles. The only appreciable difference between the XRD patterns of both samples is that the reflections of sample S1 are broader manifesting that its crystal size was significantly lower (~10 nm) than for sample R (~30 nm). It is important to note that for the DEG system, the amount of ionic liquid could be significantly reduced (DEG/IL volumetric ratio from 1:1 to 49:1) without affecting the morphological features (size and shape) of the precipitated nanoparticles in a significant manner (Table 1). This behaviour is in contrast with the EG system which required an EG/IL ratio of 1:1 to yield uniform nanoparticles (Nuñez and Ocaña 2007). Therefore, the YCl_3/DEG system is advantageous from the economic point of view, as it involves the use of a cheaper Ln precursor and a much lower amount of IL.

It must be mentioned that several rare earth fluoride particulate materials have been synthesized by precipitation in different polyols (EG, DEG and glycerol) (Wang et al. 2006; Wei et al. 2007), always resulting ill-defined precipitates consisting of strongly agglomerated nanoparticles of rather irregular shape, irrespective of the used polyol. The uniformity of the nanoparticles obtained by the here reported procedure can be explained taken into consideration the classical theory of precipitation proposed by LaMer and Dinegar (1950). This model establishes that several processes are involved in a precipitation event (mainly, formation of precipitating species, supersaturation, nucleation and nuclei growth) and that the formation of uniform particles requires a specific reaction kinetic to produce a single burst of nuclei, which will further grow by diffusion of solutes from solution to the particles surface. A way to satisfy this requirement is the slow release of the precipitating anions and/or cations to the precipitation media in an homogeneous and controlled manner (Matijević 1993), which, in our case, is guaranteed in both solvents, as the fluoride anions are liberated by the ionic liquid ($[BMIM]BF_4$) on heating at 120 °C, as a result of its hydrolysis with the hydration water molecules coming from the rare earth precursors (Nuñez and Ocaña 2007).

In order to explain the noticeable change in particle shape and microstructure associated to the change of the nature of the polyol solvent (EG or DEG) and the rare earth precursors, we must go deeper into the precipitation mechanism in both systems, which seems to be different as suggested by the different induction time (the one required for visible turbidity) observed for the EG system (40 min) in comparison with that for the DEG one

(~90 min). In fact, the rhombic morphology obtained in the EG/YOAc system, which is typical for orthorhombic YF_3 single crystals (Tao et al. 2007), is in favour of a diffusional growth of the nuclei according to th LaMer and Dinegar model (LaMer and Dinegar 1950). In contrast, a detailed observation of the spheroids at high magnification (Fig. 4) seems to indicate that these nanoparticles are formed by an ordered aggregation of small subunits, which would be in agreement with their polycrystalline nature (crystalline size is much smaller, 10 nm, than particle size, 100 × 33 nm). This mechanism of particle growth has been previously observed for several solids obtained by homogeneous precipitation in several solvents (Ocaña et al. 1995) including polyols (Ammar et al. 2004). One of the most important factors governing the mechanism of particle formation in solution is the nature of the soluble complexes precursors to precipitation, which determine their reactivity towards nuclei formation. It could be reasonably assumed that in our case, the rare earth cations form complexes with acetate anions as ligands but not with chlorides (Poul et al. 2003), as it has been demonstrated for Co(II) and Zn(II) cations in EG or DEG solutions, which would explain the important effect of the nature of the starting rare earth salt on the mechanism of particle formation. Owing to the well-known complexing ability of polyols (Wei et al. 2007; Poul et al. 2003), they may also act as complexing agents. However, they must play an additional important role in particle formation, especially in the case of growth by ordered aggregation. The formation of uniform particles through this mechanism requires a specific equilibrium between attractive and repulsive interparticle forces (Ocaña et al. 1995) whose magnitude is governed among other factors by the dielectric constant of the solvent, which is lower for DEG (31.69) than for EG (37). Therefore, the magnitude of the repulsive forces would be lower in the former solvent thus favouring the aggregation process. It should be also take into account that the viscosity of DEG is noticeably higher (35.7 MPs at 20 °C) than that of EG (18 MPs at 20 °C), which must also affect the diffusion process required for nuclei growth. All these considerations, would justify at least in part the different morphological characteristics of the particles prepared in both polyol media.

Another remarkable characteristic of both kinds of synthesized nanoparticles is their dispersability in water through a slight sonication treatment, which is essential for their potential applications in

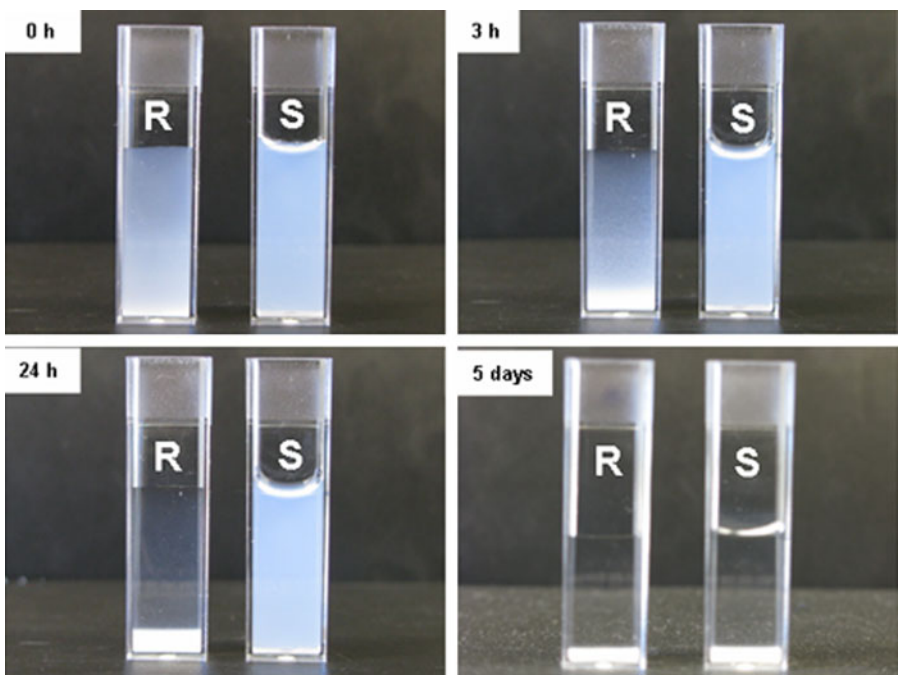

Fig. 5 Images of the suspensions prepared for samples R (R) and S1 (S) aged for different times

biotechnology. Nevertheless, it must be pointed out that as shown in Fig. 5, the spheroids remains in suspension without appreciable sedimentation a longer time (at least 24 h) than the rhombic nanoparticles (3 h). As the size of the both kinds of nanoparticles is similar, the different colloidal stability observed suggests that the nature of particle surface is different in both systems. As it will be shown later, polyols are able to adsorb on the particle surfaces preventing their aggregation (Wang et al. 2006; Wei et al. 2007). The higher efficiency of DEG as stabilizing agent detected in our system might be attributed to its larger molecular length when compared with EG.

Optical properties

The UC characteristics of YF_3:Yb^{3+},Er^{3+} co-doped nanoparticles have been investigated under CW excitation at $\lambda = 980$ nm. Although at this wavelength, both Yb^{3+} and Er^{3+} ions exhibit absorption bands, Er^{3+} contribution can be neglected due to the higher absorption cross-section of Yb^{3+} ions (Vetrone et al. 2004, Weng et al. 2009), together with the five-fold concentration factor used in this work (10% Yb^{3+} and 2% Er^{3+}). Therefore, Yb^{3+} ions are considered to be excited via direct absorption ($^2F_{7/2} \rightarrow {}^2F_{5/2}$ transition) while Er^{3+} ions are excited via energy transfer and UC mechanisms.

According to the standard description of Er^{3+}:Yb^{3+} co-doped materials (Johnson et al. 1972; Cantelar and Cussó 2003; Vetrone et al. 2004; Mai et al. 2007), after excitation, an efficient energy transfer from Yb^{3+} to Er^{3+} takes place, via the $^2F_{5/2} \rightarrow {}^2F_{7/2}$ (Yb^{3+}):$^4I_{15/2} \rightarrow {}^4I_{11/2}$ (Er^{3+}) cross-relaxation mechanism, as it is sketched in Fig. 6. The $^2F_{5/2}$ (Yb^{3+}) level is energetically resonant with the $^4I_{11/2}$ (Er^{3+}) level, so that this energy transfer is highly efficient. Then, the absorption of a second excitation photon by Yb^{3+} ions is followed by an excited state energy transfer that generates the corresponding UC process. The second energy transfer can take place via different competitive paths and, for clarity, they have been sketched separately in Fig. 6a, b.

Figure 6a illustrates how UC proceeds via a second transfer from Yb^{3+} ions, following the scheme: $^2F_{5/2} \rightarrow {}^2F_{7/2}$ (Yb^{3+}):$^4I_{11/2} \rightarrow {}^4F_{7/2}$ (Er^{3+}). This path excites the $^4F_{7/2}$ level of the Er^{3+} ion and, after an intermediate non-radiative relaxation, the $^2H_{11/2}$ and $^4S_{3/2}$ Er^{3+} levels, responsible of the two partially overlapped green emissions ($\lambda \approx 520$ and 540 nm) are populated. Alternatively, the Er^{3+} green emitting levels can partially relax non-radiatively to

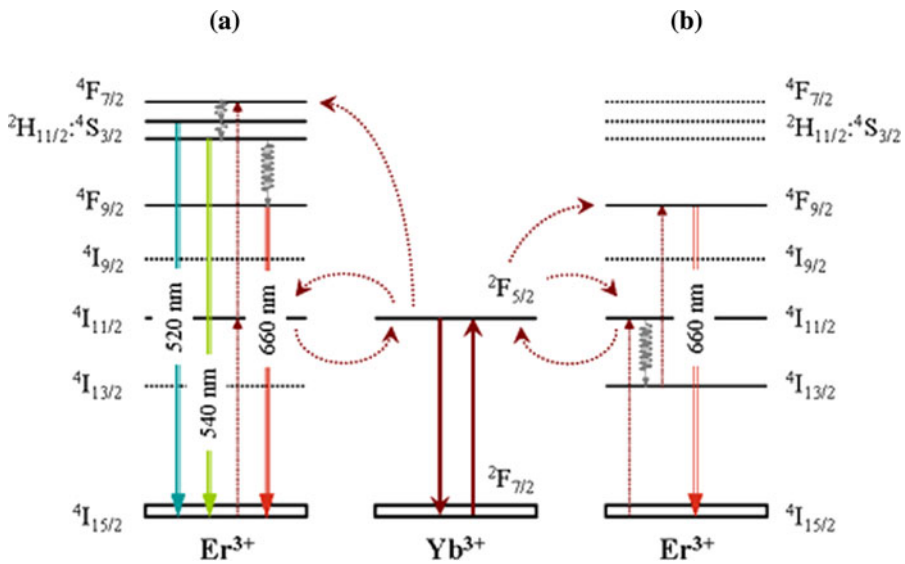

Fig. 6 Partial energy level diagram of Yb^{3+} and Er^{3+} ions, showing alternative excited state up-conversion (ETU) mechanisms. (**a**) Population of the $^4F_{7/2}$ upper Er^{3+} multiplet according to scheme: $^2F_{5/2} \rightarrow {}^2F_{7/2}$ (Yb^{3+}):$^4I_{11/2} \rightarrow {}^4F_{7/2}$ (Er^{3+}). This path activates directly the Er^{3+} green emission and also the red emission, after partial non-radiative relaxation to the $^4F_{9/2}$ multiplet. (**b**) Alternative scheme ($^2F_{5/2} \rightarrow {}^2F_{7/2}$ (Yb^{3+}):$^4I_{13/2} \rightarrow {}^4F_{9/2}$ (Er^{3+})) that populates the $^4F_{9/2}$ multiplet and increases the relative intensity of the red emission ($^4F_{9/2} \rightarrow {}^4I_{15/2}$ transition)

the $^4F_{9/2}$ level from where the emission band in the red spectral region ($\lambda \approx 650$ nm) originates.

Figure 6b illustrates an alternative UC path: the $^4I_{11/2}$ level of Er^{3+} ions relaxes partially non-radiatively to the $^4I_{13/2}$ (Er^{3+}) multiplet, from where, an energy transfer UC process can also take place according to the mechanism $^2F_{5/2} \rightarrow {}^2F_{7/2}$ (Yb^{3+}):$^4I_{13/2} \rightarrow {}^4F_{9/2}$ (Er^{3+}). This path selectively increases the population of the $^4F_{9/2}$ level and the associated red emission.

It must be noted that for the observation of the up-converted emissions in the here synthesized nanoparticles (samples R and S1) with excitation at 980 nm, a rather excessively high excitation power (>70 W/cm^2) was required. Nevertheless, once the emission was observed, the excitation power could be substantially reduced (more than two orders of magnitude) while still observing the UC emission. Therefore, in order to trigger the UC processes, it seems necessary a first high-density excitation, whose role might be related to thermal effects induced in the nanophosphors. To confirm this hypothesis, the samples were subjected to a thermal treatment for 20 min at increasing temperatures in open air, prior to optical excitation. The maximum heating temperature used was 400 °C, whereas both samples retained their morphological features after heating at this temperature (Fig. 7), a further thermal treatment at higher temperature (500 °C) resulted in a sintering process, which destroyed the particles uniformity.

In effect, as observed in Fig. 8, the characteristic Er^{3+} up-converted emissions in the visible spectral range could be now observed for the annealed rhombic (sample R) and spheroidal (sample S1) nanoparticles after 980 nm when pumping with low excitation power (<0.4 W/cm^2). This figure also shows that for both samples, the emissions bands were very similar irrespective of the target temperature, indicating that from the optical point of view, the crystal field

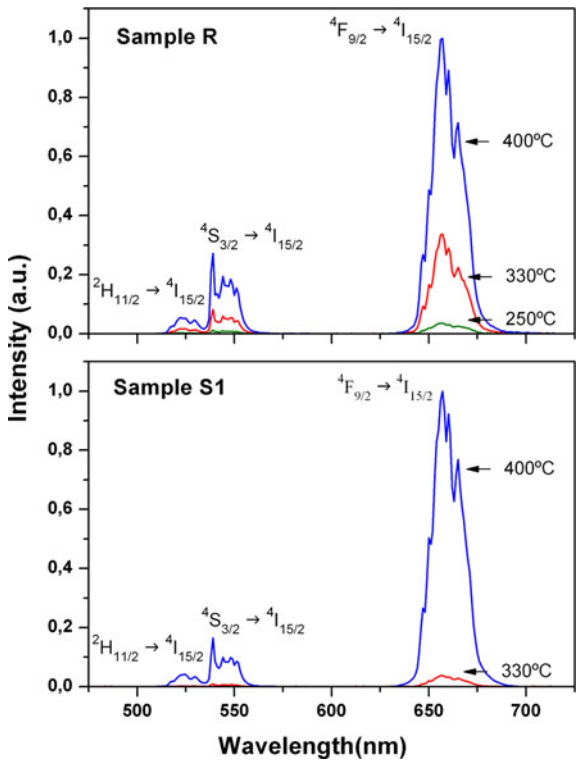

Fig. 8 Comparison of the intensities of the Er^{3+} up-conversion emissions for samples R and S1 annealed at different temperatures. The different bands have been labelled according with the corresponding optical transition, arising from different emitting Er^{3+} levels and ending in the Er^{3+} ground state ($^4I_{15/2}$)

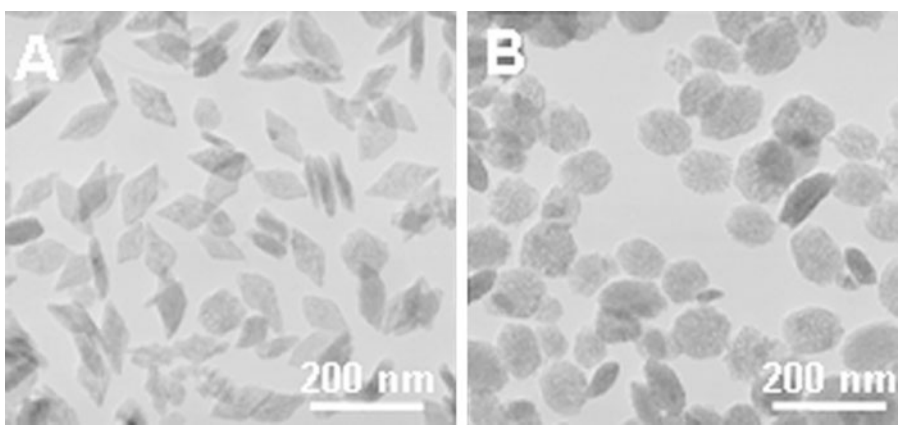

Fig. 7 TEM images of samples R (**a**) and S1 (**b**) heated at 400 °C for 20 min

environment of the lanthanide ions is not affected by this treatment, however, their relative intensity significantly increased as increasing temperature.

This behaviour seems to suggest a quenching of luminescence in the as-prepared nanophosphors, which could be related to structural defects (low crystallinity) (Cui et al. 2006) or to the presence of impurities (Kramer et al. 2004). In our case, the first possibility must be disregarded, as the XRD patterns of the samples treated at 400 °C were quite similar to those of the as-prepared samples, shown in Fig. 3, indicating that no changes of crystalline structure or crystallite size took place on heating. In order to detect the possible presence of impurities and their nature in the nanoparticles, their thermal evolution was investigated by means of TGA, infrared spectroscopy and TPD experiments.

The TGA curves obtained for samples R and S1 (Fig. 9) revealed a continuous weight loss in the range 25–400 °C, which was clearly higher for sample S1 (8.5%) than for sample R (5%). The TPD experiments (Fig. 10) revealed that these losses were mainly due to the release of water, although much smaller amounts of CO_2 and NO were also detected indicating the presence of organic groups in the nanophosphors (CO_2 may be produced from the glycols and from the 1-butyl, 2-methyl imidazolium cation of the IL, while NO must exclusively come from the later). These species were clearly detected in the DRIFT spectra of the as-prepared samples (Fig. 11), which in both cases displayed two intense bands centred at 3,400 (very broad) and 1,630 cm^{-1}

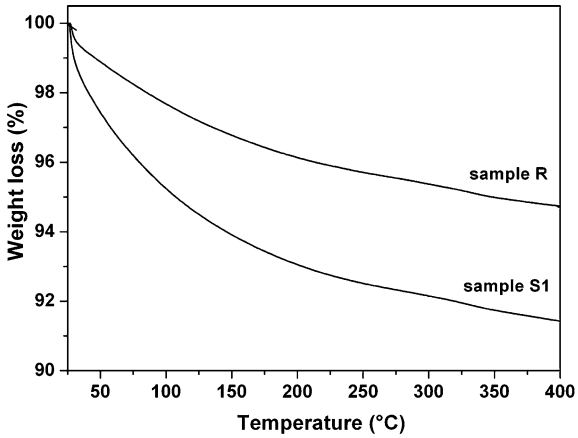

Fig. 9 Termogravimetric analyses for samples R and S1

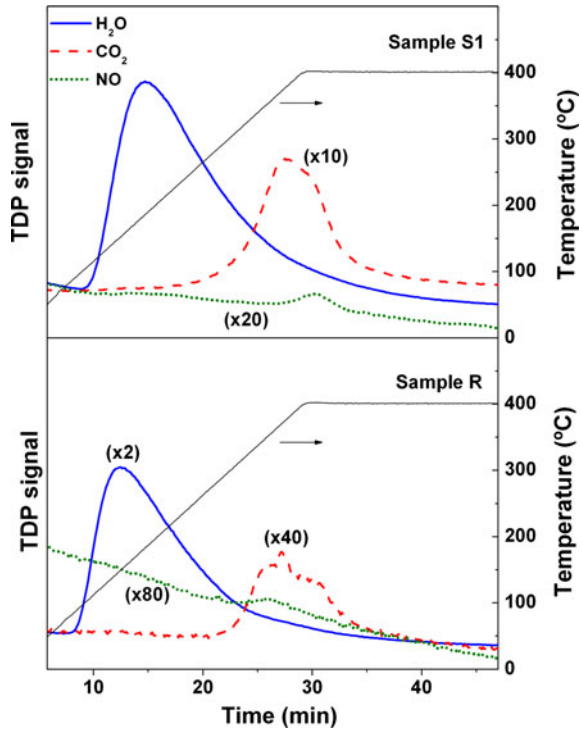

Fig. 10 TDP signals obtained for samples R and S1. Some signals have been magnified for a better observation

mainly due to the OH stretching and H–O–H bending vibrations of water, respectively, along with some very weak absorptions in the 1,500–1,000 cm^{-1} region, which could be attributed to EG (sample R) (Matsuura and Miyazawa 1967) or DEG (sample S1) (Caruntu et al. 2002). It is very important to note that after heating at 400 °C, the water bands completely disappeared for sample R, whereas those due to the organic groups were replaced by others more intense in the 1,500–1,300 cm^{-1} region, which can be assigned to carboxylate anions (Colthup et al. 1990), indicating that the oxidation and further release of the adsorbed organic species was incomplete in this temperature range. It should be noted that these residual carboxylate groups might be beneficial for the functionalization required for the biological applications of the nanophosphors (Kong et al. 2007). The only noticeable difference observed for the thermal behaviour of sample S1 with respect to sample R is that water was not completely released in the former at 400 °C (Fig. 11).

These results indicate that the presence of OH groups in the neighbourhood of the lanthanide ions is

most probably responsible for the quenching of luminescence observed for the as-prepared samples. Thus, it is well documented that the high-energy vibrational modes of the OH group enhance the multiphonon relaxation of the rare-earth excited states, reducing the overall luminescence quantum yield (Cusso et al. 2001; Xu et al. 2005; De et al. 2006; Schäfer et al. 2007). In the particular case of UC emission from Yb,Er-doped materials, the multiphonon relaxation must affect a variety of levels involved in the different stages of the transfer processes. In particular, considering the two different UC schemes sketched in Fig. 6, there are many possible effects enhanced by the multiphonon relaxations. For instance, the green emitting Er^{3+} levels ($^2H_{11/2}$ and $^4S_{3/2}$) may be quenched, while promoting the red emission arising from the $^4F_{9/2}$ level (Fig. 6a). Also, the non-radiative component could enhance the $^4I_{11/2} \rightarrow {}^4I_{13/2}$ transition, increasing the relative importance of the alternative transfer process indicated in Fig. 6b. Overall, the $^4I_{13/2}$ Er^{3+} level can be quenched to the ground state ($^4I_{15/2}$) producing a strong reduction in the efficiency of all related luminescent processes. Therefore, the elimination of the OH content in the nanoparticles, can account for the dramatic increase of the luminescence intensity after the annealing treatments.

It is also important to mention that as illustrated in Fig. 12 where the integrated intensity of the green and red emission bands is plotted as function of annealing temperature, the rhombic nanoparticles begun to show a significant emission intensity after being annealed at lower temperature (around 250 °C) than the spheroids (≥330 °C). In addition, the intensity of the emissions reached an almost constant value around 380 °C for the rhombus, while for spheroids a stable intensity was not attained, at least in the temperature range considered. This behaviour is most probably also related to the higher relative efficiency of the UC luminescence found for the rhombic nanophosphors when compared with the

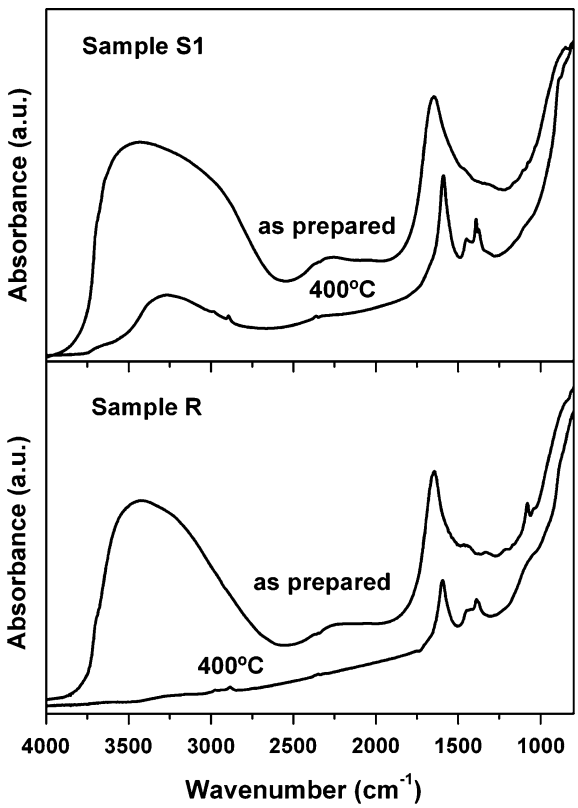

Fig. 11 DRIFTS spectra of samples R and S1 as-prepared and after heating at 400 °C for 20 min

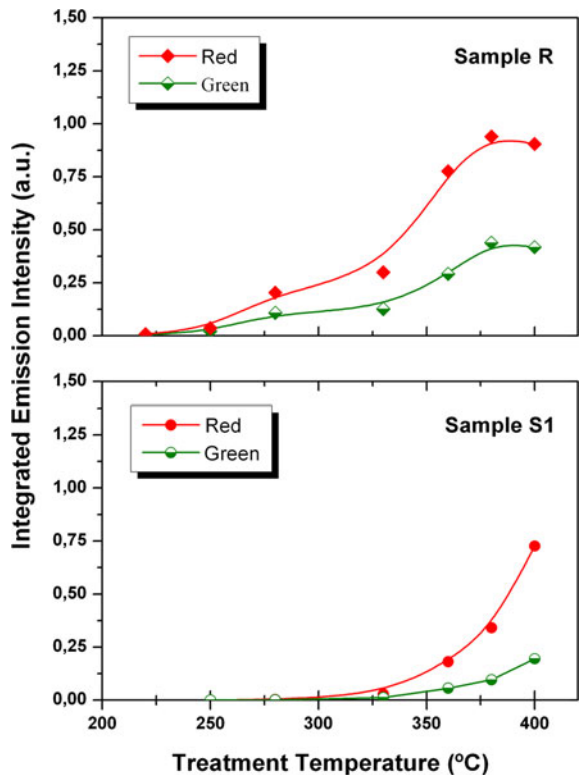

Fig. 12 Integrated intensity of the green and red emissions plotted as function of annealing temperature for samples R and S1

spheroids after annealing at 400 °C as deduced from Fig. 13. In this figure, the UC-emissions of the nanoparticles of both shapes normalized to the IR emission at $\lambda \approx 1.5$ μm arising from the $^4I_{13/2} \rightarrow {}^4I_{15/2}$ transition of Er^{3+} ions are shown. Therefore, it compares directly the fraction of photons that these ions emit in the visible or in the IR spectral region. As it can be clearly appreciated, the rhombic nanoparticles exhibit superior UC efficiency than spheroids (approximately a factor two higher integrated intensity), which could be justified in view of the presence of the residual amount of water detected by DRIFTS in the latter after heating, whereas it was completely eliminated in the rhombic nanoparticles (Fig. 11). A possible influence of the lower crystallite size of the nanospheroids detected by XRD (Fig. 3) on its lower efficiency can not be discarded.

It should also be noted that the annealing treatments affects the relative intensity of the red and green emissions. In particular, the spheroidal nanoparticles experience a noticeable change in the spectra, and the green-to-red ratio (GRR) of the UC emissions varies from about 0.50 for the low-temperature annealed spheroids to about 0.13 for those annealed at 400 °C. The appearance of the samples changes consequently from a yellowish-green hue, for samples treated at low temperatures, to an orange hue when annealed at 400 °C (Fig. 14). Rhombic nanoparticles were less affected and the GRR changes from 0.30 for low-temperature annealed samples to 0.23 for those treated at 400 °C. Although, in general (Mai et al. 2007; Kramer et al. 2004; Xu et al. 2005; De et al. 2006; Schäfer et al. 2007; Capobianco et al. 2002), the elimination of impurities is accompanied of a higher GRR value, in the present work, we observe a reduction in the GRR values for the annealed samples. This could be understood considering that the main effect of the suppression of OH groups is the overall increase of the luminescence efficiency, possibly related to the increase in the population of $^4I_{13/2}$ (Er^{3+}) multiplet, which should increase the relative efficiency of the red UC. Although this is a possible explanation, further experimental work is needed in order to confirm this mechanism.

Finally, it is important to note that once the samples have been activated by the annealing treatment, the samples were still stable in water suspension and the up-converted emission was visible even with the naked eye, as illustrated in Fig. 15 for sample R, which makes these nanophosphors suitable for biotechnological applications.

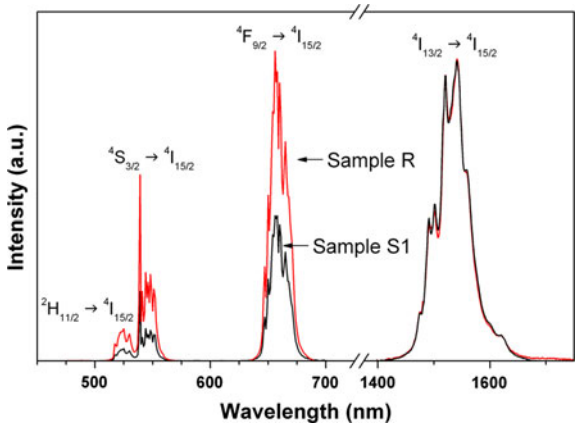

Fig. 13 Comparison of the intensities of the Er^{3+} up-conversion emissions of samples R (*rhombic*) and S1 (*spheroids*). Both samples have been previously annealed at 400 °C and the spectra have been normalized to the Er^{3+} IR emission at $\lambda \approx 1.5$ μm ($^4I_{13/2} \rightarrow {}^4I_{15/2}$ transition). It can be observed that sample R exhibits a higher up-conversion efficiency

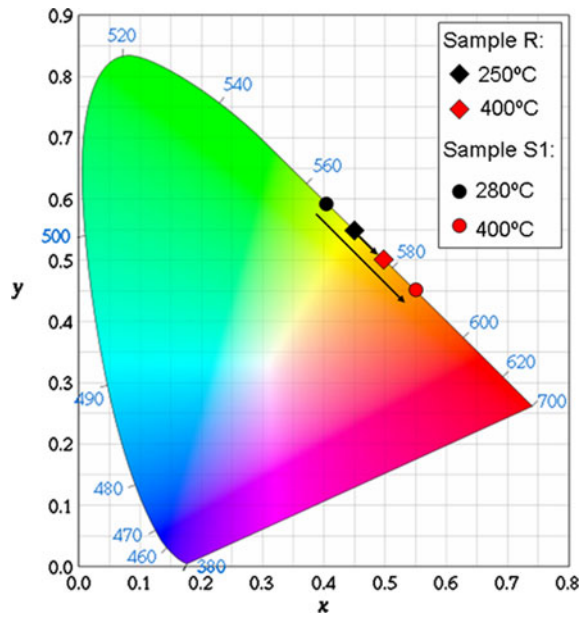

Fig. 14 CIE colour coordinates for samples R and S1 heated at different temperatures for 20 min

Fig. 15 Dispersion of rhombic Er,Yb;YF_3 nanophosphors (sample R) in water showing UC luminescence sample when excited at 980 nm: (*left*) total UC, (*centre*) UC viewed through a red filter, (*right*) UC viewed through a green filter. The photograph has been taken using a LUMIX DMC-digital camera (1 s exposure at ISO 400)

Conclusions

Water-dispersible and uniform Er,Yb-doped YF_3 UC nanophosphors ($\sim$100 nm) of various morphologies (rhombic and spheroidal) could be synthesized through a homogeneous precipitation process at 120 °C in polyol (EG or DEG) solutions containing different lanthanide salts and an ionic liquid (1-butyl, 2-methylimidazolium tetrafluoroborate) as fluoride source. The shape of the obtained nanoparticles was mainly determined by the nature of both, the solvent and the lanthanide precursor, which is attributed to differences in their formation mechanism. The UC processes for both kinds of synthesized nanoparticles (rhombic and spheroidal) were found to be quenched in the as-prepared samples due to the multiphonon relaxation of the rare-earth excited states enhanced by the high-energy vibrational modes of OH groups coming from adsorbed water. Nevertheless, these groups could be released (completely in the nano-rhombus and partially in the nanospheroids) by thermal annealing at 400 °C without altering particle size and shape, which resulted in a strong luminescence. The UC efficiency of the heated nanoparticles was found to be higher for the rhombus than for the spheroids, which was mainly attributed to the incomplete release of water in the latter case. Finally, both kinds of nanophosphors were water dispersible and their up-converted emission was visible even with the naked eye, which makes these nanophosphors suitable for biotechnological applications.

Acknowledgements This work has been funded by the Spanish Ministerio de Educación y Ciencia (MEC) (grant MAT2008-02166), Junta de Andalucía (grant FQM3579) and Comunidad de Madrid (grant MICROSERES S-0505/TIC/0191). N.O. Nuñez thanks the Spanish Research Council for funding her contract under the JAE program. M. Quintanilla wants to thank the Spanish Ministerio de Educación y Ciencia for an FPU fellowship. We also acknowledge Mr. Victor González for his technical assistance in the DRIFT and TPD measurements.

References

Ammar S, Jouini N, Fievet F, Stephan O, Marhic C, Richard M, Villain F, Cartier dit Moulin Ch, Brice S, Sainctavit Ph (2004) Influence of the synthesis parameters on the cation distribution of $ZnFe_2O_4$ nanoparticles obtained by forced hydrolysis in polyol medium. J Non-Cryst Solids 345 & 346:658–662

Cantelar E, Cussó F (2003) Comparative up-conversion mechanisms in Er^{3+}/Yb^{3+} co-doped $LiNbO_3$. J Lumin 102–103:525–531

Cao C, Qin W, Zhang J, Zhang J, Wang Y, Jin Y, Wei G, Wang G, Wang L (2008) Multicolor up-conversion emissions of $Tm^{3+}/Er^{3+}/Yb^{3+}$ Tri-doped YF3 phosphors. J Nanosci Nanotechnol 8:1384–1387

Capobianco JA, Vetrone F, Boyer JC, Speghini A, Bettinelli M (2002) Enhancement of red emission ($^4F_{9/2} \rightarrow {}^4I_{15/2}$) via upconversion in bulk and nanocrystalline cubic $Y_2O_3:Er^{3+}$. J Phys Chem B 106:1181–1187

Caruntu D, Remond Y, Chow NH, Jun MJ, Caruntu G, He J, Goloverda G, O'Connors C, Kolesnichenko V (2002) Reactivity of 3d transition metal cations in diethylene glycol solutions. Synthesis of transition metal ferrites with the structure of discrete nanoparticles complexed with long-chain carboxylate anions. Inorg Chem 41:6137–6146

Colthup NB, Daly LH, Wiberley SE (1990) Introduction to infrared and Raman spectroscopy. Academic Press, San Diego, p 318

Cui Y, Fan X, Hong Z, Wang M (2006) Synthesis and luminescence properties of lanthanide(III)-doped YF_3 nanoparticles. J Nanosci Nanotechnol 6:830–836

Cusso F, Lifante G, Muñoz JA, Cantelar E, Nevado R, Cino A, De Micheli MP, Sohler W (2001) Spectroscopic investigation of proton exchanged Er-doped lithium niobate waveguides. Radiat Eff Defect Solids 155:217–221

De G, Qin W, Zhang J, Zhao D, Zhang J (2005) Bright-green upconversion emission of hexagonal LaF_3: Yb^{3+}, Er^{3+} nanocrystals. Chem Lett 34:914–991

De G, Qin W, Zhang J, Zhang J, Wang Y, Cao C, Cui Y (2006) Effect of OH− on the upconversion luminescent efficiency of $Y_2O_3:Yb^{3+}$, Er^{3+} nanostructures. Solid State Commun 137:483–487

Downing E, Hesselink L, Ralston J, Macfarlane R (1996) A three-color, solid-state, three-dimensional display. Science 273:1185–1189

Johnson LF, Guggenheim HJ, Rich TC, Ostermayer FW (1972) Infrared-to-visible conversion by rare-earth ions in crystals. J Appl Phys 43:1125–1167

Kong DY, Wang ZL, Lin CK, Quan ZW, Li YY, Li CX, Lin J (2007) Biofunctionalization of CeF_3:Tb^{3+} nanoparticles. Nanotechnology 18:075601

Kramer KW, Biner D, Frei G, Gudel HU, Hehlen MP, Luthi SR (2004) Hexagonal sodium yttrium fluoride based green and blue emitting upconversion phosphors. Chem Mater 16:1244–1251

LaMer VK, Dinegar RJ (1950) Theory, production and mechanism of formation of monodispersed hydrosols. J Am Chem Soc 72:4847–4854

Li Z, Zhang Y (2008) An efficient and user-friendly method for the synthesis of hexagonal-phase $NaYF_4$:Yb, Er/Tm nanocrystals with controllable shape and upconversion fluorescence. Nanotechnology 19:345606

Mai HX, Zhang YW, Sun LD, Yan CH (2007) Highly efficient multicolor up-conversion emissions and their mechanisms of monodisperse $NaYF_4$:Yb, Er core and core/shell-structured nanocrystals. J Phys Chem C 111:13721–13729

Matijević E (1993) Preparation and properties of uniform size colloids. Chem Mater 5:412–426

Matsuura H, Miyazawa T (1967) Infrared spectra and molecular vibrations of ethylene glycol and deuterated derivatives. Bull Chem Soc Jpn 40:85–94

Nuñez NO, Ocaña M (2007) An ionic liquid based synthesis method for uniform luminescent lanthanide fluoride nanoparticles. Nanotechnology 18:455606

Nuñez NO, Míguez H, Quintanilla M, Cantelar E, Cussó F, Ocaña M (2008) Synthesis of spherical down- and up-conversion $NaYF_4$-based nanophosphors with tunable size in ethylene glycol without surfactants or capping additives. Eur J Inorg Chem 4517–4524

Ocaña M, Rodriguez-Clemente R, Serna CJ (1995) Uniform colloidal particles in solution: formation mechanisms. Adv Mater 7:212–216

Poul L, Ammar S, Jouini N, Fievet F (2003) Synthesis of inorganic compounds (metal, oxide and hydroxide) in polyol medium: a versatile route related to the sol–gel process. J Sol-Gel Sci Technol 26:261–265

Schäfer H, Ptacek P, Kömpe K, Haase M (2007) Lanthanide-doped $NaYF_4$ nanocrystals in aqueous solution displaying strong up-conversion emission. Chem Mater 19:1396–1400

Scheps R (1996) Prog upconversion laser processes. Prog Quantum Electron 20:271–358

Shalav A, Richards BS, Trupke T, Krämer KW, Güdel HU (2005) Application of $NaYF_4$:Er^{3+} up-converting phosphors for enhanced near-infrared silicon solar cell response. Appl Phys Lett 86:013505

Stouwdam JW, van Veggel FCJM (2002) Near-infrared emission of redispersible Er^{3+}, Nd^{3+}, and Ho^{3+} doped LaF_3 nanoparticles. Nano Lett 2:733–737

Sun YJ, Chen Y, Tian LJ, Yu Y, Kong XG, Zhao JW, Zhang H (2007) Controlled synthesis and morphology dependent upconversion luminescence of $NaYF_4$:Yb, Er nanocrystals. Nanotechnology 18:275609

Tao F, Wang Z, Yao L, Cai W, Li X (2007) Synthesis and photoluminescence properties of truncated octahedral Eu-doped YF_3 submicrocrystals or nanocrystals. J Phys Chem 111:3241–3245

Vetrone F, Boyer JC, Capobianco JA, Speghini A, Bettinelli M (2004) Significance of Yb^{3+} concentration on the upconversion mechanisms in codoped Y_2O_3:Er^{3+}, Yb^{3+} nanocrystals. J Appl Phys 96:661–667

Wang F (2006) Facile synthesis of water-soluble LaF_3:Ln^{3+} nanocrystals. J Mater Chem 16:1031–1034

Wang L, Li Y (2007) Controlled synthesis and luminescence of lanthanide doped $NaYF_4$ nanocrystals. Chem Mater 19:727–734

Wang ZL, Quan ZW, Jia PY, Lin CK, Luo Y, Chen Y, Fang J, Zhou W, O′Connor CJ, Lin J (2006) A facile synthesis and photoluminescent properties of redispersible CeF_3, CeF_3:Tb^{3+}, and CeF_3:Tb^{3+}/LaF_3 (core/shell) nanoparticles. Chem Mater 18:2030–3037

Wang J, Bo S, Song L, Hu J, Liu X, Zhen Z (2007) One-step synthesis of highly water-soluble LaF_3:Ln^{3+} nanocrystals in methanol without using any ligands. Nanotechnology 18:465606

Wang GF, Qin WP, Zhang JS, Zhang JS, Wang Y, Cao CY, Wang LL, Wei GD, Zhu PF, Kim R (2008) Enhancement of violet and ultraviolet upconversion emissions in Yb^{3+}/Er^{3+}-codoped YF_3 nanocrystals. Opt Mater 31:296

Wang GF, Qin WP, Wei GD, Wang LL, Zhu PF, Kim RJ, Zhang DS, Ding FH, Zheng KZ (2009) Synthesis and upconversion luminescence properties of YF_3:Yb^{3+}/Tm^{3+} octahedral nanocrystals. J Fluor Chem 130:158–161

Wei Y, Lu F, Zhang X, Chen D (2007) Polyol-mediated synthesis of water-soluble LaF_3:Yb, Er upconversion fluorescent nanocrystals. Mater Lett 61:1337–1340

Weng F, Chen D, Wang Y, Yu Y, Huang P, Lin H (2009) Energy transfer and up-conversion luminescence in Er^{3+}/Yb^{3+} co-doped transparent glass–ceramic containing YF_3 nanocrystals. Ceram Int 35:2619–2623

Xu S, Fang D, Zhang Z, Jiang Z (2005) Effect of OH− on upconversion luminescence of Er^{3+}-doped oxyhalide tellurite glasses. J Solid State Chem 178:2159–2162

Yan R, Li Y (2005) Down/up conversion in Ln^{3+}-doped YF_3 nanocrystals. Adv Funct Mater 15:763–770

Yi G, Chow G (2005) Colloidal LaF_3:Yb, Er, LaF_3:Yb, Ho and LaF_3:Yb, Tm nanocrystals with multicolor upconversion fluorescence. J Mater Chem 15:4460–4464

Yi GS, Chow GM (2006) Synthesis of hexagonal-phase $NaYF_4$: Yb, Er and $NaYF_4$: Yb, Tm nanocrystals with efficient up-conversion fluorescence. Adv Funct Mater 16: 2324–2329

Yi G, Lu H, Zhao S, Ge Y, Yang W, Chen D, Guo L (2004) Synthesis, characterization, and biological application of size-controlled nanocrystalline $NaYF_4$:Yb, Er infrared-to-visible up-conversion phosphors. Nanoletters 4: 2191–2196

Zhang T, Guo H, Qiao YM (2009) Facile synthesis, structural and optical characterization of LnF_3:Re nanocrystals by ionic liquid-based hydrothermal process. J Lumin 129: 861–866